Electrocatalytic oxygen evolution with pure and substituted $M_6(SR)_{12}$ (M = Pd, Fe, Rh) complexes

De Nyago Tafen[a,c,*], Douglas R. Kauffman[b], Dominic R. Alfonso[b]

[a] National Energy Technology Laboratory, United States Department of Energy, 1450 Queen Ave SW, Albany, Oregon 97321, United States

[b] National Energy Technology Laboratory, United States Department of Energy, 626 Cochrans Mills Road, Pittsburgh, Pennsylvania 15241, United States

[c] AECOM, P.O. Box 1959, Albany, Oregon 97321, United States

* Corresponding author.

E-mail address: denyago.tafen@netl.doe.gov (D. N. Tafen)

Abstract

The development of new technologies to generate fuels from water splitting requires highly active and cost-effective catalysts. Organometallic complexes have attracted considerable interests due to their scientific significance and their ability to efficiently photo- and electro-catalyze H_2 and O_2 evolution reactions. Here, we combine density functional theory (DFT) and computational electrochemical analysis to predict the oxygen evolution reaction (OER) activity of a series of organometallic complexes containing methyl thiol ligands and compare it to that of Ni complex. We find that the OER activity versus the diameter of the hexagonal ring shows a maximum activity which corresponds to that of Ni complex. We also find an existence of linear correlations of the adsorption energies with the ring diameter of the oxidized complexes. In an effort to improve the OER activity of these complexes, we substitute a metal cation with Ni, and we show that Ni-doped complexes give rise to smaller overpotentials. The enhanced overpotential can be explained in terms of the overall affinity of active sites for reactive species resulting in a shift of their binding energies. Finally, we find that substituting Fe atoms into small organometallic Ni complex does not appear to have the same influence that has been observed in bulk materials. We believe these predictions will help guide catalyst design by identifying active and robust OER catalysts, capable to reduce the energy required for the anodic water oxidation. Reducing anodic overpotentials will help reduce the overall energy requirements of both H_2 evolution and CO_2 reduction systems.

Keywords: Electrocatalysis; oxygen evolution reaction; water splitting; density functional theory; organometallic; reaction profile

1. Introduction

Growing energy demands, and environment concerns have prompted global efforts to explore alternative energy sources separate from fossil fuels. One effort consists of electrochemically splitting water to hydrogen and oxygen. To achieve this, earth-abundant, non-precious electrocatalyst materials at the anode and cathode are critical. At the anode, molecular oxygen in addition to protons and electrons are produced through electrochemical oxygen evolution reaction (OER). However, the high-energy requirements of the OER (due to the high overpotential, >0.35 V) produce challenges for large-scale deployment [1-4].

In an effort to find stable earth-abundant electrocatalysts, researchers have turned their attention to ligand-protected metal nanoclusters [5-7]. Among them, small organometallic complexes have gained special attention because of their size, their precisely known crystal structure, their structural similarity to the active sites in heterogeneous catalysts [8], and their photocatalytic and electrocatalytic hydrogen generation properties [9-12]. The small size of these organometallic complexes makes it possible for experimentalists and computational theorists to study a nearly identical system and accurately identify structure-property relationships. Recently, we have used a combination of experimental and computational techniques to study the OER activity of an organometallic nickel complex containing phenylethyl thiol ligands [13]. This particular Ni species was interesting because it demonstrated stable OER activity that rivaled state-of-the-art Ir-based OER catalysts. Our success with nickel thiolate complex prompted us to expand our studies to other metal thiolate complexes denoted as $M_6(SCH_3)_{12}$, with M = Pd, Fe, Rh. Palladium and iron thiolate complexes have been synthesized and fully characterized experimentally [14-16]. Their structures are similar to that of $Ni_6(SR)_{12}$, and they form a tiara-like structure stabilized by metal-S π bonds [17]. These complexes are robust and possess large

HOMO-LUMO gap [15]. The six metal atoms are arranged in a nearly hexagonal ring with twelve bridging sulfur atoms (six above and six below the plane). Palladium thiolate complex has been used as a precursor to prepare monodisperse PdS nanoclusters [18]. However, there are currently no reports of OER activity of these metal thiolate clusters. To the best of our knowledge there is no literature data on $Rh_6(SR)_{12}$. However, rhodium thiolate complexes have shown to efficiently catalyze the hydroformylation of olefins [19-21].

In this work, we report the electrochemical and electrocatalytic behavior of a series of organometallic metal complexes $M_6(SCH_3)_{12}$ using computational techniques. The behavior of these complexes has allowed for the formulation of a correlation between the OER activity and the diameter of the ring formed by the metal and sulfur atoms due to the existence of linear correlations between the adsorption energies of the reaction intermediates and the diameter of the ring. Furthermore, we investigate the effect of substituting a metal atom with Ni on the overpotential for OER. Surface modification by doping has shown to improve reaction kinetics and reduce overpotentials [22-24]. For example, it was demonstrated theoretically that doping the (0001) surface of hematite with Ni and Co lowers the overpotential, resulting to an increase of the OER activity [22]. This increase was attributed to an improvement in the reactions thermodynamics due to the relative stabilities of holes on the active O anions. Fe substitution in nickel complex was also investigated. Unlike Fe substitution in Ni complex, the substitution of Rh and Pd with a Ni atom reduces the overpotentials.

2. Computational methodology

For the simulations performed here we used DFT methods as implemented in the Vienna *Ab Initio* Simulation Package (VASP) code, version 5.3.3 [25, 26]. We used the generalized

gradient approximation formulation of Perdew, Burke and Enzerhoff (PBE) [27] to evaluate the exchange-correlation energy. The same functional was used in our previous work on $Ni_6(SCH_3)_{12}$, where our theoretical predictions were in excellent agreement with experiments, showing the reliability of PBE for these kinds of systems. We have also performed validation calculations with a more expensive and less approximate hybrid functional. Projected augmented wave (PAW) pseudopotentials were used to described the electron-ion interaction [28]. Among the available PAW potentials supplied with the VASP code, we used Pd_pv 06Sep2000 ($4p^6 5s^2 4d^8$), Fe_pv 06Sep2000 ($3p^6 4s^2 3d^6$), Rh_pv 06Sep2000 ($4p^6 5s^2 4d^7$), Ni_pv 06Sep2000 ($3p^6 4s^2 3d^8$), O 08Apr2002 ($2s^2 2p^4$), S 17Jan2003 ($3s^2 3p^4$), C 08Apr2008 ($2s^2 2p^2$), and H 15Jun2001 (s^1). The Kohn-Sham equations were solved in a plane wave basis set with a kinetic energy cutoff of 500 eV. Our starting structure is $Ni_6(SCH_3)_{12}$ from our previous work, where nickel is replaced by the transition metal M (M = Fe, Pd, Rh). Due to computational cost associated with the number of atoms, the ligand fragment is represented by ($-SCH_3$). Previous works using this simplified representation of ligand fragment yielded good agreement with experiments [13, 29, 30]. A single cluster of the resulting complex, $M_6(SCH_3)_{12}$, was placed at the center of a cubic box and periodic boundary conditions were applied in all three directions. To avoid spurious interactions between images of the system at least 14 Å of vacuum was added in x, y, and z directions. Spin polarization calculations were carried out using Γ-point. The FM and AFM states were tested for Fe, and the Fe cations were considered to be in their high spin states. The ionic degrees of freedom were relaxed until the residual forces were less than 0.03 eV/Å.

We modeled the OER thermochemistry with a commonly accepted mechanism that includes four sequential one electron oxidation steps (Equations I-IV) [31-33]. This mechanism

has been widely applied to various catalytic processes and has been successful in capturing their reactivity trends [13, 22, 31-35].

(I) $H_2O\,(l) + * \leftrightarrow OH_{ads} + H^+ + e^-$

(II) $OH_{ads} \leftrightarrow O_{ads} + H^+ + e^-$

(III) $O_{ads} + H_2O\,(l) \leftrightarrow OOH_{ads} + H^+ + e^-$

(IV) $OOH_{ads} \leftrightarrow * + O_2\,(g) + H^+ + e^-$

The terms OH_{ads}, O_{ads}, and OOH_{ads} in these equations represent the OER intermediates adsorbed on a free metal site denoted by (*). In this mechanism, a water molecule undergoes two successive oxidations to form O_{ads} by releasing protons and electrons. The adsorbed oxygen then reacts with another water molecule to form OOH_{ads} followed by an O_2 gas release.

The standard equilibrium potentials of the aforementioned electrochemical steps were computed using the computational hydrogen electrode (CHE) model [36]. This model that has been successfully applied to OER on metal oxide surfaces [33] and nanoclusters [13, 37]. By referencing ($H^+ + e^-$) to that of H_2 in standard hydrogen electrode (SHE), i.e., $G(H^+ + e^-) = \frac{1}{2}G(H_{2(g)})$ at p = 101325 Pa, T = 298 K, pH = 0, the electrochemical steps can be treated as if they are chemical in nature. The effect of electrode potential ($U \neq 0$ V vs SHE) at pH =0 can be accounted for by including a $-eU$ term in their reaction free energy. Therefore, for oxidation steps (I-IV) the reaction free energies follow:

$$\Delta G_I = G_{OH_{ads}} + \frac{1}{2}G_{H_2} - G_{H_2O} - G_* - eU \qquad (1)$$

$$\Delta G_{II} = G_{O_{ads}} + \frac{1}{2}G_{H_2} - G_{OH_{ads}} - eU \qquad (2)$$

$$\Delta G_{III} = G_{OOH_{ads}} + \frac{1}{2}G_{H_2} - G_{O_{ads}} - G_{H_2O} - eU \qquad (3)$$

$$\Delta G_{IV} = G_* + G_{O_2} + \frac{1}{2} G_{H_2} - G_{OOH_{ads}} - eU \qquad (4)$$

The Gibbs free energy *G* for the gaseous species is obtained by adding zero-point energy (E_{zpe}), thermal energy (E_{th}), *PV* work term, and entropic contributions (*TS*) to the electronic energy (E_{el}) from DFT calculations [38]: $G = E_{el} + E_{zpe} + E_{th} + PV - TS$. The E_{th} term is the sum of translational ($U_{trans} = \frac{3}{2} RT$), rotational ($U_{rot}(\text{nonlinear molecule}) = \frac{3}{2} RT$; $U_{rot}(\text{linear molecule}) = RT$) and vibrational contributions ($U_{vib} = R\sum_i \frac{h\nu_i / k_B}{e^{h\nu_i / k_B T} - 1}$) to the internal energy. The *PV* term can be replaced by *RT* assuming an ideal gas. E_{zpe} and the vibrational component of the entropies and ZPE corrections of the OER intermediates were calculated from the vibrational frequencies using standard methods [39]. The entropy contribution (vibrational entropy) is given by:

$$S = k_B \sum_i^{3N} \left[-ln\left(1 - e^{-\beta\varepsilon_i}\right) + \frac{\beta\varepsilon_i}{e^{\beta\varepsilon_i - 1}} \right] \qquad (5)$$

where $\varepsilon_i = h\nu$. The vibrational frequencies are derived from the Hessian matrix using finite difference methods. For the adsorbed species, the substrates are fixed in their relaxed positions and the normal mode frequencies of the adsorbates are computed. For the OER intermediates, the *PV* term is ignored due to its small contribution as do the translational and rotational components of E_{th} and *S*. Thus, only the vibrational component of E_{th} and *S* are considered.

The OER onset potential (U_{onset}), which is the least potential necessary for all reaction steps to become downhill, was determined from the free energy diagram [31, 34]. By definition, $U_{onset} = max(\Delta G_I, \Delta G_{II}, \Delta G_{III}, \Delta G_{IV})/e$, where ΔG_i is the reaction free energy of step (*i*) and *e* the charge of an electron. To account for solvation effects we applied a method developed by Hennig *et al*. and implemented in VASP [40, 41]. The method uses a Poisson-Boltzmann implicit solvent

model. The background dielectric constant of water was $\varepsilon_b = 80$ with a cutoff charge density of 0.0025 $Å^{-3}$ and the cavitation energies were evaluated using a surface tension of 0.525 meV/$Å^2$.

Table 1

Average calculated ring diameters in Å (D_M for M_6 ring, D_{MS} for M_6S_{12} ring), atomic distances in Å ($d_{M\text{-}M}$, $d_{M\text{-}S}$), and bond angles in degrees, α_i, for bare and $M_6(SCH_3)_{12}$-O_5. Data for nickel complex is from Ref [13]. Data for iron is for the FM configurations.

	D_M (Å)	D_{MS} (Å)	$d_{M\text{-}M}$ (Å)	$d_{M\text{-}S}$ (Å)	$\alpha_{M\text{-}M\text{-}M}$	$\alpha_{M\text{-}S\text{-}M}$	$\alpha_{S\text{-}M\text{-}S}$
$Pd_6(SCH_3)_{12}$	6.36	6.90	3.18	2.36	120º	84.7º	94.8º
$Pd_6(SCH_3)_{12}$-O_5	6.96	7.44	3.48	2.34	120º	88.2º	96º
$Fe_6(SCH_3)_{12}$	4.85	5.86	2.43	2.24	120º	65.6º	94.3º
$Fe_6(SCH_3)_{12}$-O_5	4.85	6.06	2.43	2.25	120º	65.3º	95.9º
$Rh_6(SCH_3)_{12}$	5.55	6.42	2.78	2.32	120º	73.5º	96.9º
$Rh_6(SCH_3)_{12}$-O_5	5.54	6.69	2.79	2.31	120º	74.4º	96.5º
$Ni_6(SCH_3)_{12}$ [13]	5.91	6.41	2.95	2.20	120º	84º	95º
$Ni_6(SCH_3)_{12}$-O_5 [13]	6.59	6.94	3.30	2.19	120º	88º	97º

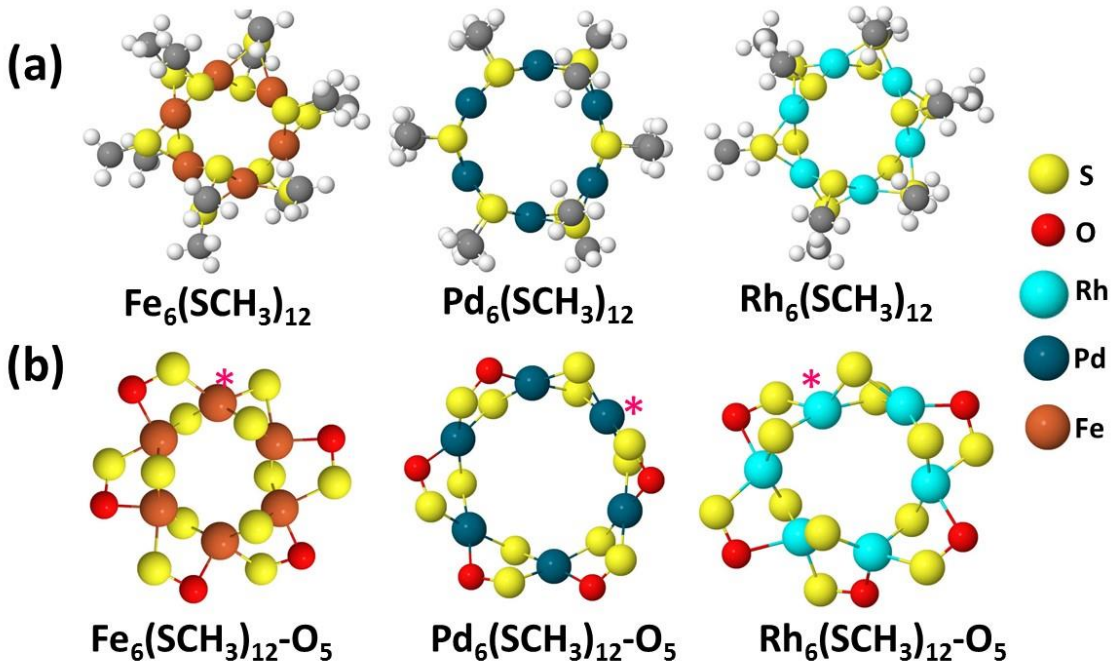

Fig. 1. Predicted structure of (a) bare $M_6(SCH_3)_{12}$ and (b) oxygen-covered $M_6(SCH_3)_{12}$-O_5 (M = Fe, Pd, Rh). We omit the ligands from panel b for clarity and the active sites for OER are marked with an asterisk. For cell boundaries see Fig. 1 in Ref [42].

3. Results and discussion

3.1. Structural Properties of $M_6(SCH_3)_{12}$

Fig. 1 presents the predicted structural geometries of $M_6(SCH_3)_{12}$ (M = Fe, Pd, Rh) obtained via DFT simulations. The metal complexes contain six metal atoms in a hexagon with nearly D_3 symmetry. Twelve S atoms containing organic ligands complete the structure. Selected computed internal geometric parameters for these organometallic complexes are summarized in Table 1. The diameters of the Fe_6, Rh_6, and Pd_6 ring are 4.85, 5.55 and 6.36 Å, respectively. These diameters are proportional to the closest metal-metal atomic distance, $d_{M\text{-}M}$, and larger metal-metal atomic distances ($d_{M\text{-}M}$) produced larger M_6 diameter rings. The M-M-M angles ($\alpha_{M\text{-}M\text{-}M}$) remain similar for all the metal complexes. However, the M-S-M angles ($\alpha_{M\text{-}S\text{-}M}$) vary in the same manner as $d_{M\text{-}M,}$ with the smallest value corresponding to $Fe_6(SCH_3)_{12}$. DFT calculations of the $Pd_6(SCH_3)_{12}$ yielded a structure that is consistent with single crystal X-ray crystallography [15, 18]. For example, Yang et al. [18] found an average Pd-Pd and Pd-S internuclear distances of 3.11 and 2.32 Å, respectively, which are in very good agreement with our DFT predicted values of 3.18 and 2.36 Å. The experimental average Pd-Pd-Pd and Pd-S-Pd angles are about 120º and 84.4º, respectively, compared to our predicted values of 120º and 84.7º.

For the iron complex structure, we have considered various spin configurations of Fe, such as, configurations with spins antiferromagnetically aligned (AFM), configurations with spins ferromagnetically aligned (FM), and configurations with four Fe spin up and two Fe spin down

(IS). The lowest energy configurations correspond to the AFM and FM with an energy difference of approximately 4 meV (see Table 1 in Ref [42]). Overall, our DFT results agree well with the experimental crystal structure of $[Fe(\mu_2\text{-}SEt)_2]_6$ reported by Wang et al. [16]. The experimental average Fe-Fe-Fe and S-Fe-S angles are about 120° and 95.6°, respectively, compared to DFT predictions of 120° and 94.3° in FM configurations and 120° and 97.2° in AFM configurations (see Table 2 in Ref [42]). However, the average Fe-Fe internuclear distance differs from the experimental values by approximately 0.5 and 0.4 Å in the FM and AFM configurations, respectively. The difference might be due to the variations of the μ-S bridging modes, Fe-S-Fe angles and Fe-S distances. No experimental parameters exist for $Rh_6(SCH_3)_{12}$ in the literature so we compare the predicted parameters to $Pd_6(SCH_3)_{12}$ and $Fe_6(SCH_3)_{12}$. The predicted Rh-S-Rh angle of 73.5° is higher than the Fe-S-Fe and smaller than the Pd-S-Pd, whereas the predicted S-Rh-S angle of 96.9° is higher than both the S-Fe-S and S-Pd-S angles. The atomic distances or internuclear distances ($d_{M\text{-}M}$ and $d_{M\text{-}S}$) follow the trend Fe < Rh < Pd.

Our previous work suggested the reactive surface of $Ni_6(SCH_3)_{12}$ was oxygen-covered at OER potentials [13], and we expect the same for the complexes considered here. The oxidized structures follow a scheme developed in the Nørskov's group [43], where metal ions are covered with oxygen to a certain critical coverage. For $M_6(SCH_3)_{12}$, that critical coverage is 5/6 of a monolayer of oxygen. The FM alignment of all Fe ions in $Fe_6(SCH_3)_{12}\text{-}O_5$ is found to be energetically more favorable than the AFM and IS alignments by more than 120 meV (Table 1 in Ref [42]). From now on we discuss only the results for the FM case. Fig. 1b shows the predicted structures of O-covered $M_6(SCH_3)_{12}$ denoted $M_6(SCH_3)_{12}\text{-}O_5$. One metal atom (denoted as *) is left vacant to represent the OER active site. Similar to nickel case, oxygen in each organometallic complex prefers to adopt a two-fold binding configuration between the metal and sulfur atoms.

The average M-O bond length is 2.02, 2.13 and 2.19 Å for Fe-O, Pd-O and Rh-O, respectively. The average S-O bond length in all three complexes is approximately 1.58 Å. Our calculations show that one-fold oxygen adsorption at Fe, Pd, and Rh site is energetically less favorable by 0.41, 2.59, and 1.31 eV per O atom, respectively. One can see that upon adsorption of oxygen atoms, the cyclic hexagonal like architecture is preserved with minor structural distortions. For the O-covered Fe and Rh complexes, the most prominent change is the expansion of the Fe-S and Rh-S diameter ring by 0.20 and 0.27 Å, respectively. In the case of $Pd_6(SCH_3)_{12}$-O_5, oxygen adsorption induced an elongation of the closest Pd-Pd distance by 0.30 Å leading to an expansion of the Pd and Pd-S diameter rings by approximately 0.6 Å compared to O-free $Pd_6(SCH_3)_{12}$ (Table 1). We confirmed the quality of our PBE predictions by performing single-structure total energy calculations using the HSE06 hybrid exchange-correlation functional that contains exact exchange and it is less approximate but very expensive [44]. In this formalism, the screening parameter (μ) that controls the range separation between the short-range and long-range part of the Coulomb kernel is set to 0.20 $Å^{-1}$. PBE and HSE06 results of the adsorption energies of intermediates on $Pd_6(SCH_3)_{12}$-O_5 are in quantitative and qualitative agreement, as reported in Table 3 of Ref [42].

3.2. Oxygen Evolution Reaction on $M_6(SCH_3)_{12}O_5$

Fig. 2 presents free energy diagrams for OER at O-covered $Fe_6(SCH_3)_{12}O_5$, $Pd_6(SCH_3)_{12}O_5$, and $Rh_6(SCH_3)_{12}O_5$, respectively. For each complex, the initial surface state for OER includes free H_2O molecules and a vacant metal site (denoted as *). At the initial condition (* + $2H_2O$), ΔG for the reaction is defined as ΔG = 0. The free energy for each elementary step is calculated and presented in Table 2. The numbers in bold represent the most positive reaction energies. In the absence of applied potential, the OER reactions need 4.96 eV of energy to proceed,

which corresponds to an electrochemical reaction potential of 1.24 V (4.96 eV / $4e^-$). This predicted value agrees very well with the expected water splitting formal potential of 1.23 V. All electrochemical reaction steps in the free energy diagram are uphill (endothermic) at U=0, except for the formation of O_2 which becomes downhill (exothermic) for $Pd_6(SCH_3)_{12}O_5$. The predicted structures for the adsorbed intermediates are presented in Fig. 2, and in Figs. 2 and 3 of Ref [42].

Table 2

Gibbs free energy change (ΔG) for each OER reaction step O-covered $M_6(SCH_3)_{12}O_5$ (M = Fe, Pd, Rh); all ΔG values are in eV. The numbers in bold represent the most positive reaction energies. Data for nickel complex is from Ref [13]. Results for AFM- $Fe_6(SCH_3)_{12}O_5$ are presented in Table 4 of Ref [42].

		ΔG *per* step (eV)			
Step	Process	$Fe_6(SCH_3)_{12}O_5$	$Pd_6(SCH_3)_{12}O_5$	$Rh_6(SCH_3)_{12}O_5$	$Ni_6(SCH_3)_{12}O_5$ [13]
I	H_2O (l) → OH_{ads}	0.65	**2.34**	1.41	1.63
II	OH_{ads} → O_{ads}	0.59	1.99	0.77	**1.68**
III	O_{ads} → OOH_{ads}	**2.63**	1.02	**1.96**	1.44
IV	OOH_{ads} → O_2 (g)	1.09	-0.39	0.82	0.21
Total ΔG	$2H_2O$ (l) → O_2 (g)	4.96	4.96	4.96	4.96

The U_{onset} and potential determining step (PDS) for OER at each complex were determined from OER free energy diagrams and highlighted with bold text in Table 2. Our results predict -OOH_{ads} formation (step III) to be the PDS for both $Fe_6(SCH_3)_{12}O_5$ and $Rh_6(SCH_3)_{12}O_5$, with U_{onset} = 2.63, and 1.96 V, respectively. In contrast, our results predict OH_{ads} formation to be a PDS for $Pd_6(SCH_3)_{12}O_5$ with U_{onset} = 2.34 V. The results from our previous study are also contained in

Table 2, with $Ni_6(SCH_3)_{12}O_5$ predicted to have a PDS involving O_{ads} formation and a U_{onset} = 1.68 V [13]. We point out the predicted $Ni_6(SCH_3)_{12}O_5$ values were in excellent agreement with experimental U_{onset} values. Overall, our results predict U_{onset} to increase as Ni < Rh < Pd < Fe.

The OER intermediates structures as predicted by DFT simulations show that these complexes are stable and robust. They retained their atomic arrangement throughout the OER process. The same characteristics were observed in $Ni_6(SCH_3)_{12}$ [13]. As in the case of $Ni_6(SCH_3)_{12}$, the O_{ads} intermediate for all the organometallic complexes studied binds in a one-fold coordination with the metal atom.

A comparison to our recent experimental and theoretical work on organometallic nickel complex reveals that the PDS depends on the transition metal (TM). One might have expected that for all the organometallic complexes studied the PDS for the OER process would have been the same. This difference might be due to the binding affinity of the TM with the intermediates. It was shown that the strength of the interaction between the adsorbates and the TM depends critically on the degree of filling of the anti-bonding states, which in turn depends on the position of the *d* states relative to the Fermi level [45, 46]. On the basis of the Sabatier principle, the interaction between the catalyst and the reactant should be neither too strong nor too weak [47, 48]. To elucidate the difference in the OER activity, we turned to the adsorption energies of the intermediates (Fig. 3). The smaller the adsorption energy the stronger the chemical interaction between the adsorbate and the substrate. Our results show a weakening in the adsorption energies of O, OH, and OOH in the following order Pd < Ni < Rh < Fe, with the strongest adsorption on Fe resulting to a less favorable formation of OOH_{ads} from O.

The linear relationships between the binding energies of the intermediates of these complexes closely resemble that reported for various oxide surfaces [33], and for transition metals

and their oxides [43, 49]. Fig. 3a shows that the binding energies of OH_{ads} and O_{ads} linearly correlated with a slope of 0.52 and an intercept of 0.16 eV compared to a slope of 0.50 and an intercept of 0.44 eV obtained by Man et al. on transition metals and their oxides including perovskites [33]. The difference in intercepts is due to the difference in binding sites. The scaling between $\Delta E_{OOH_{ads}}$ and $\Delta E_{OH_{ads}}$ (Fig. 3b) with a slope of ~ 1.0, and an intercept of 3.25 eV agrees with the existence of an universal scaling relation between the binding energies of the intermediates in an OER electrocatalysis [33]. Fig. 4 in Ref [42] shows the scaling relationships between ΔG_{OH} and ΔG_O, and ΔG_{OOH} and ΔG_{OH}. Using the fitting parameters described above we constructed a 2D contour map of the onset potentials as a function of ΔG_{OH} and (ΔG_O - ΔG_{OH}), and the resulting data is plotted in Fig. 4. According to the scaling relationships in Fig. 4 in Ref [42], the closer (ΔG_O - ΔG_{OH}) is with respect to 3.020/2 = 1.510 eV, the smaller the reaction potential. In Fig. 4, Ni complex is located near that optimum value with (ΔG_O - ΔG_{OH}) = 1.68 eV, which results to maximum activity compared to others. Therefore, Ni provides optimal relative binding strengths of *OH and *OOH among the complexes studied. Employing the above scaling relations increases U_{onset} of $Rh_6(SCH_3)_{12}O_5$ by 0.29 V and decreases that of $Fe_6(SCH_3)_{12}O_5$ by 0.20 V while leaving $Ni_6(SCH_3)_{12}O_5$ and $Pd_6(SCH_3)_{12}O_5$ potentials unchanged. Our contour map also shows that it is possible to tune the activity even higher by reducing the onset potential.

It was also demonstrated that structural parameters (such as lattice parameters, strain, nearest neighbors, etc.) can affect surface reactivity by modifying the electronic band structure et surface bonds, and therefore adsorption energies. These parameters have often been used as descriptors to control the activity of electrocatalysts [50-52]. Calle-Vallejo *et al*. used nearest neighbors counting to find optimal active sites on heterogeneous catalysts [51], while Escudero-Escribano et al. obtained a relationship between the oxygen reduction reaction activity and the

bulk lattice parameter in Pt-lanthanide alloy electrocatalysts [52]. To explore whether there is a connection between the OER activity and the structural parameters, we plot in Fig. 5 the OER onset potential as a function of the $M_6(SCH_3)_{12}$-O_5 ring diameter (D_{MS}) of the oxidized complex. Our results show a maximum at D_{MS} = 6.94 Å which corresponds to $Ni_6(SCH_3)_{12}O_5$. We also find an existence of linear correlations between OH_{ads} and OOH_{ads}, ΔG_{OH} and ΔG_{OOH}, and D_{MS} (Fig. 5b), where increased D_{MS} corresponds to weaker ΔG_{OH} and ΔG_{OOH}. Furthermore, D_{MS} correlates strongly with OER onset potential. These observations suggest that the $M_6(SCH_3)_{12}$-O_5 ring diameter of the oxidized complex can be used as descriptors of the OER activity.

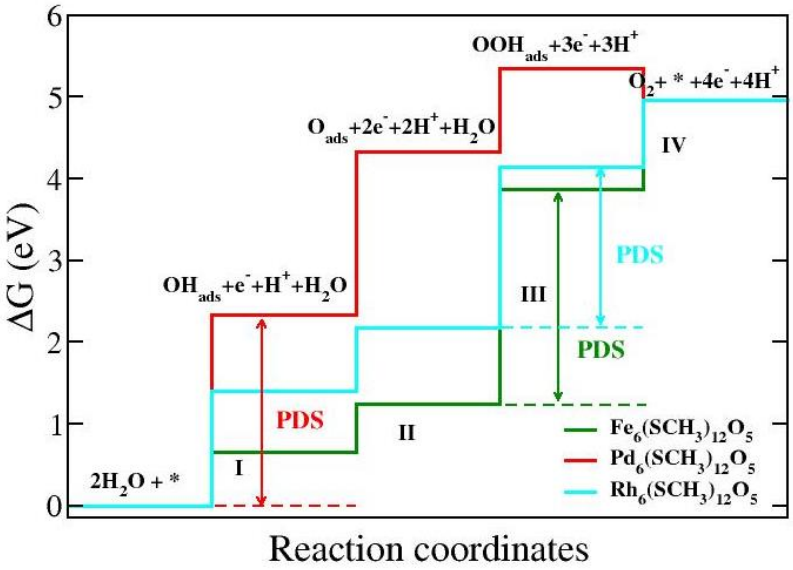

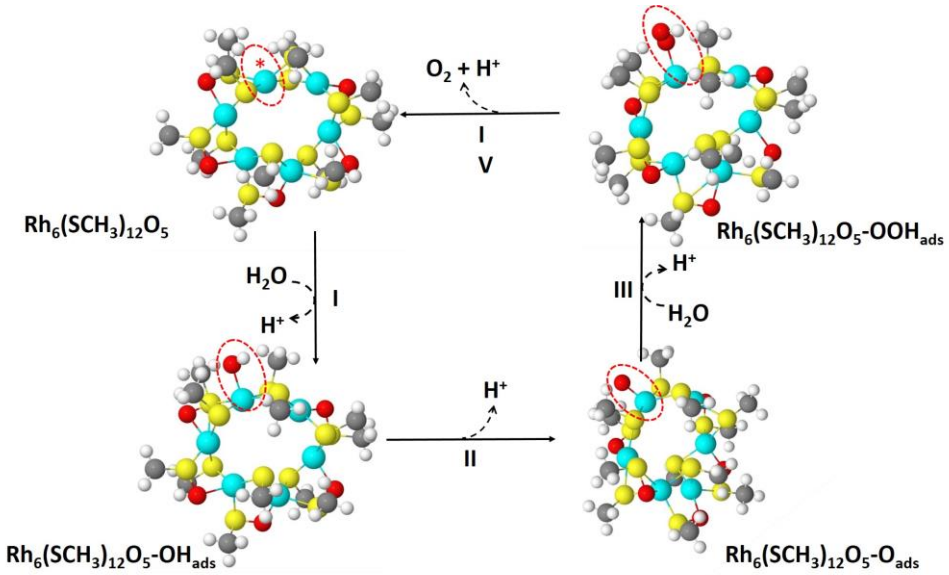

Fig. 2. Schematic of the OER on $M_6(SCH_3)_{12}O_5$ (M = Fe, Pd, Rh) at room temperature and zero applied potential. (Top) Gibbs free energy of reactions. (bottom) Predicted structures for all intermediates on $Rh_6(SCH_3)_{12}O_5$. The OER reaction intermediates on $M_6(SCH_3)_{12}O_5$ (M= Fe, Pd) are presented in Figs. 2 and 3 in Ref [42]. The adsorbed OER intermediates are highlighted with red dashed circle.

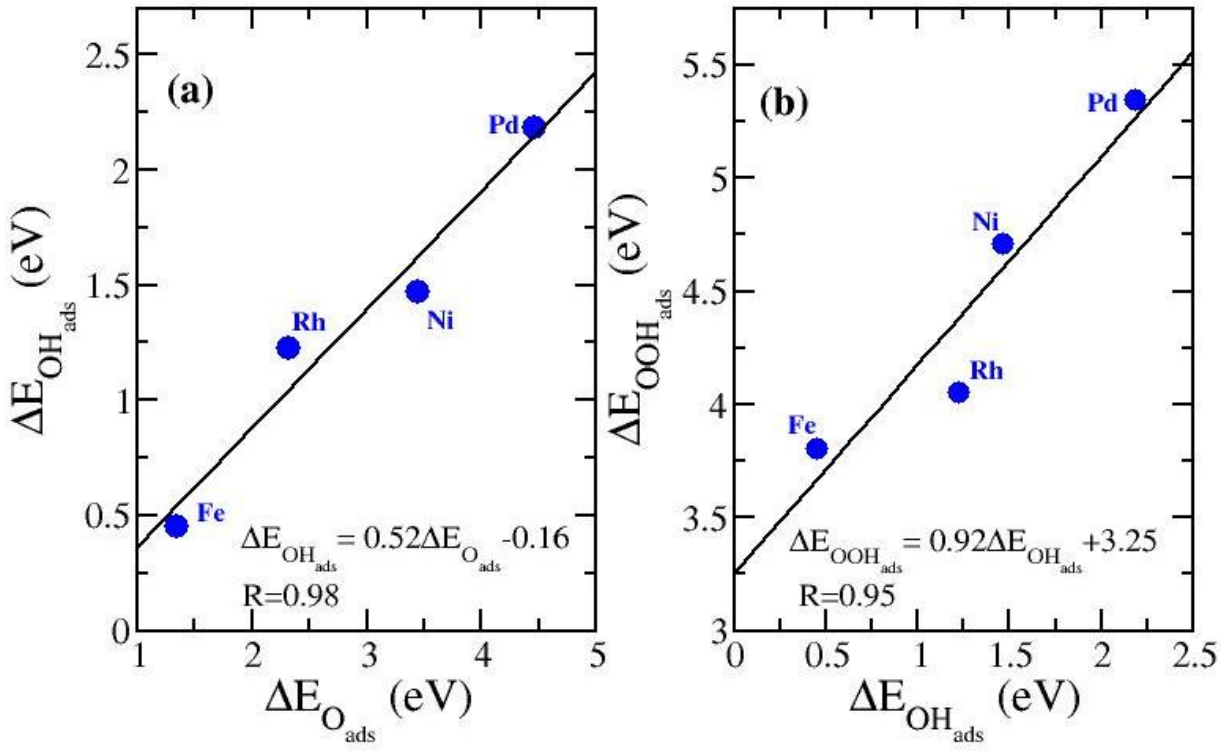

Fig. 3. DFT energies of intermediates O_{ads}, OH_{ads}, and OOH_{ads} on $M_6(SCH_3)_{12}$-O_5 (M = Fe, Rh, Pd, Ni) organometallic complexes. Least-squares fits are provided together with the correlation coefficients, R.

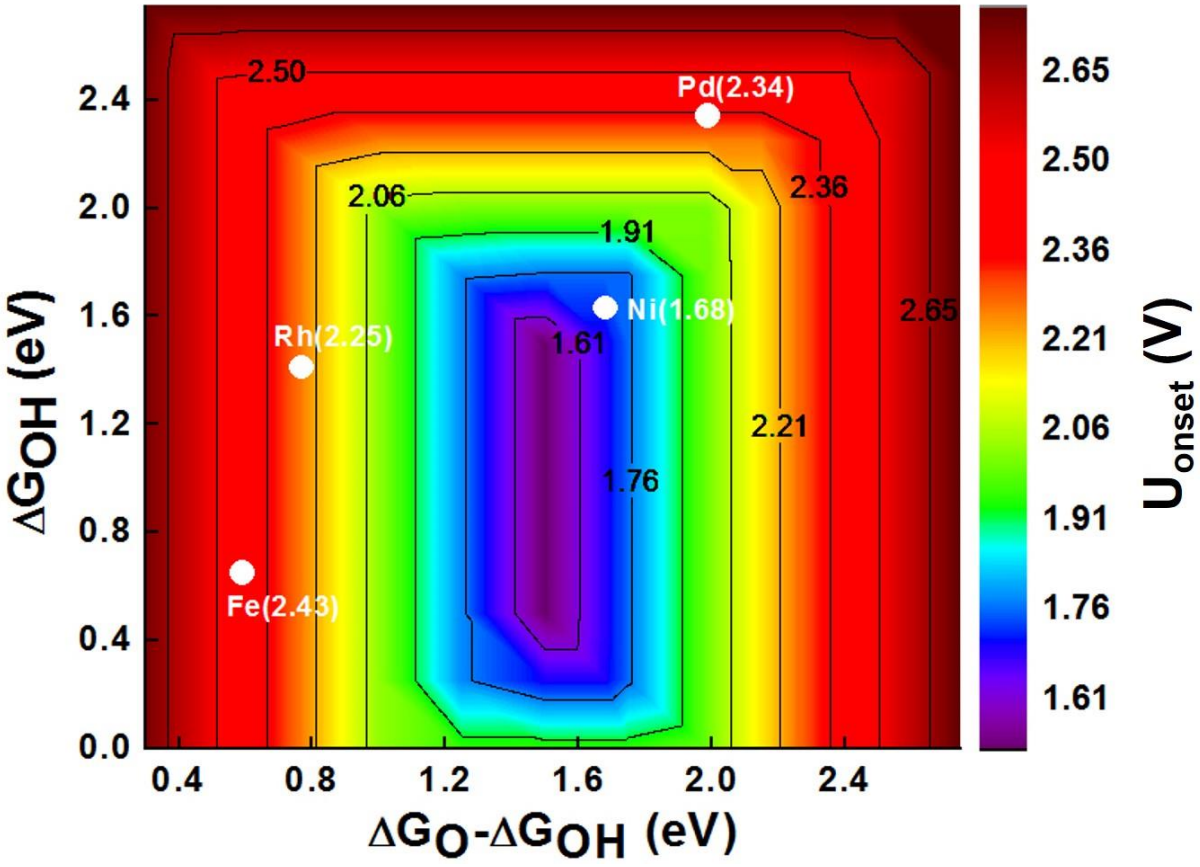

Fig. 4. 2D contour map of onset potentials, U_{onset}, for the oxidized $M_6(SCH_3)_{12}$ (M = Fe, Rh, Ni, Pd) organometallic complexes as function of $\Delta G_O - \Delta G_{OH}$ and ΔG_{OH}. We have used the fitting parameters of the binding energies to construct the map.

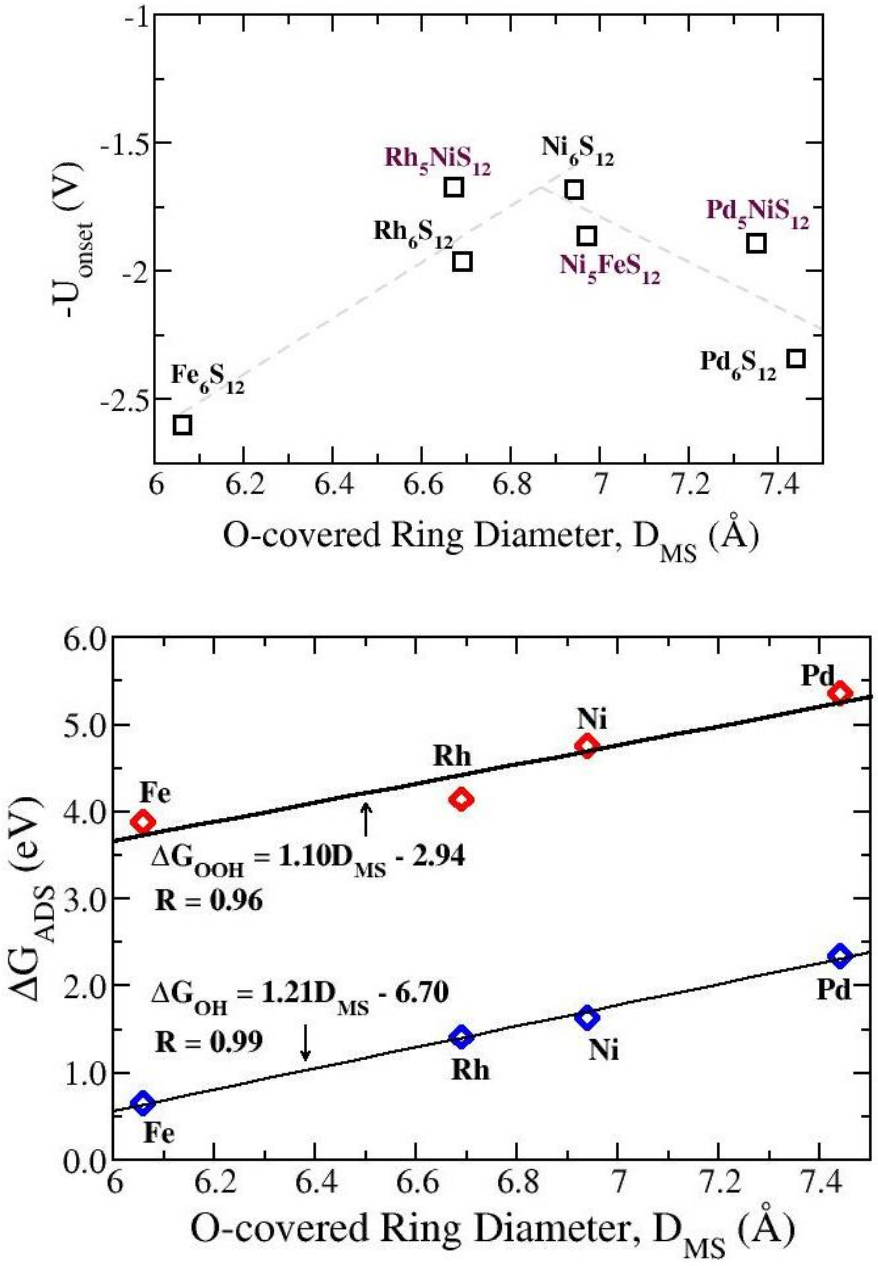

Fig. 5. (a) Plot of the onset potential, U_{onset}, versus the diameter of the O-covered M_6S_{12} (M = Fe, Rh, Ni, Pd) ring. Also included are the doped complexes (maroon color). The dashed lines are to guide the eyes. (b) Trends in ΔG_{OH} and ΔG_{OOH} described by the diameter of the O-covered M_6S_{12} ring, D_{MS}. Least-squares fits are provided together with the correlation coefficients.

Table 3

Calculated Bader charges q (in units of electrons) for the active site M with and without the adsorbates as well as for the O in the adsorbates *O, *OH, and *OOH on $M_6(SCH_3)_{12}O_5$ (M = Fe, Rh, Pd, Ni)

$M_6(SCH_3)_{12}$-O_5	(*)	*O		*OH		*OOH	
	q	q	q:O	q	q:O	q	q:O
$Fe_6(SCH_3)_{12}$-O_5	0.561	1.066	-0.762	0.874	-1.549	0.975	-0.785
$Rh_6(SCH_3)_{12}$-O_5	0.294	0.768	-0.616	0.593	-1.448	0.644	-0.697
$Pd_6(SCH_3)_{12}$-O_5	0.264	0.589	-0.694	0.502	-1.469	0.444	-0.668
$Ni_6(SCH_3)_{12}$-O_5 [13]	0.428	0.729	-0.681	0.683	-1.545	0.657	-0.747

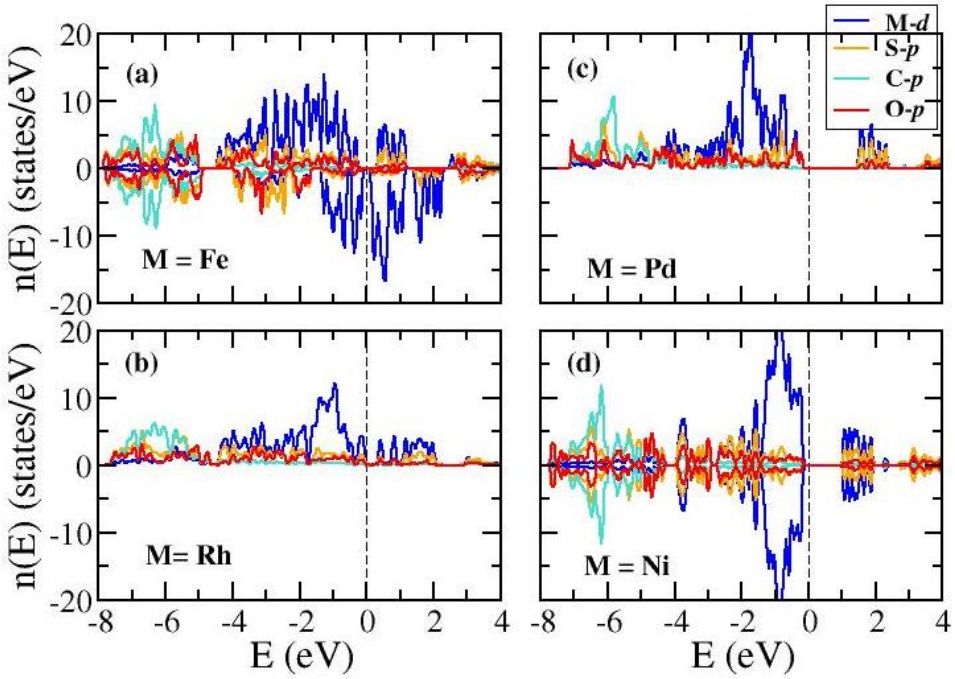

Fig. 6. Projected density of states for $M_6(SCH_3)_{12}O_5$ (M = Fe, Rh, Pd, Ni) under vacuum. Positive values represent majority spin DOS whereas negative values represent minority spin DOS. The energies are shifted so that the Fermi level is at zero.

We also analyze the electronic density of states and Bader charges [53] of these complexes. In Fig. 6, we plot the projected density of states (PDOS) of $M_6(SCH_3)_{12}O_5$ (M = Fe, Rh, Pd, Ni). In all cases, the valence band region close to the Fermi level is formed mostly by 3*d* metal sub-bands which interact with those dominated by 2*p*- and 3*p*- states of the oxygen and sulfur with small C 2*p* contribution. This indicates hybridization of the metal *d*-band with S and O *p*-states to form strong bonds. The lesser metal features at the bottom region of the valence band indicates a weaker hybridization between the metal and oxygen/sulfur as compared to the sulfur 3*p* and 2*p* of oxygen and carbon. In $Fe_6(SCH_3)_{12}O_5$, both majority and minority spin channels exhibit a small bandgap. For the rest, a clear gap is also visible above the Fermi level. In Table 3 we show the effective Bader charges of the metals and the O anions in the adsorbates. Relative to the bare case, a significant increase of charge is predicted on the metal reaction center upon adsorption. From another perspective, adsorption implies oxidation of the metal center with the O atom to which the metal is bonded receiving much of the charge. Overall, the Fe-O bond has more ionic character compared to those that involve the other transition metal cations.

3.3. Oxygen Evolution Reaction on substituted-organometallic complexes

Previous studies have shown that surface modification by doping can improve electrochemical OER performance, and incorporating Fe heteroatoms into Ni-based electrocatalysts can dramatically reduce U_{onset} and increase electrocatalytic reaction rates [35, 54]. We carried out simulations to determine the effects of substitutional doping of a metal active site by a Ni cation. We limit ourselves to the case where Ni dopant is bonded directly to the reaction site. Fig. 7a contains the DFT predicted structures of Ni-substituted $Pd_5Ni(SCH_3)_{12}O_5$, and $Rh_5Ni(SCH_3)_{12}O_5$. Nickel was considered the active site in both $Pd_5Ni(SCH_3)_{12}O_5$, and

$Rh_5Ni(SCH_3)_{12}O_5$, and both Ni and Fe active sites were considered on $Ni_5Fe(SCH_3)_{12}O_5$ (see Fig. 7a). The active sites in $Ni_5Fe(SCH_3)_{12}O_5$ are denoted :Fe or :Ni, and active sites are marked with an asterisk in all structures. Interestingly, the $Fe_5Ni(SCH_3)_{12}O_5$ structure was not stable upon adsorption of OH and OOH intermediates. Specifically, intermediate adsorption resulted in severe structural distortion and cleavage of Ni-S bonds (see Fig. 5 in Ref [42]).

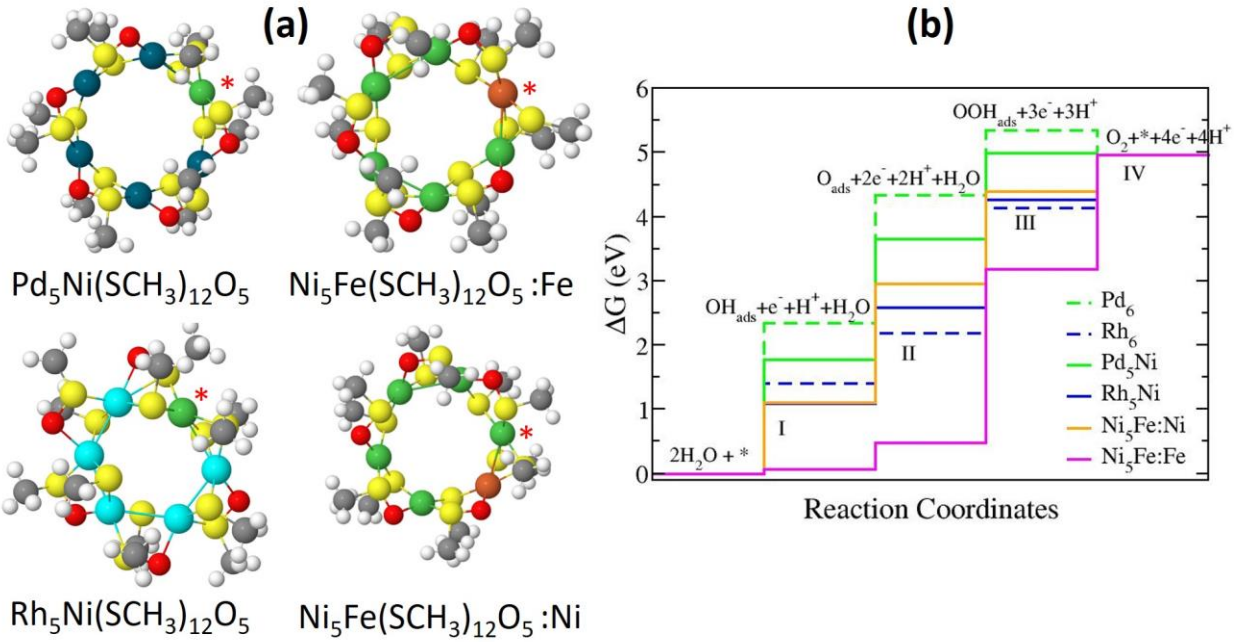

Fig. 7. (a) Structures of oxygen-covered doped-organometallic complexes. The asterisk denotes the OER active site which is an O-free metal atom. **(b)** Free energies of reactions for the doped-organometallic complexes compared to the pure.

Table 4

ΔG_i and U_{onset} for the OER on O-covered, substituted-organometallic complexes. U_{onset} are highlighted in bold text.

ΔG	$Pd_5Ni(SH_3)_{12}O_5$	$Rh_5Ni(SCH_3)_{12}O_5$	$Ni_5Fe(SCH_3)_{12}O_5$:Ni	$Ni_5Fe(SCH_3)_{12}O_5$:Fe
ΔG_I	1.77	1.09	1.10	0.06
ΔG_{II}	**1.89**	1.50	**1.86**	0.42
ΔG_{III}	1.33	**1.67**	1.43	**2.70**
ΔG_{IV}	-0.03	0.71	0.58	1.78
U_{onset}	1.89	1.67	1.86	2.70

Fig. 7b and Table 4, contain the free energy diagrams and associated ΔG for each step for each substituted metal complex. DFT calculations predict O_{ads} formation (step II) as a PDS for $Pd_5Ni(SCH_3)_{12}O_5$ and $Ni_5Fe(SCH_3)_{12}O_5$:Ni, and OOH_{ads} formation (step III) for $Rh_5Ni(SCH_3)_{12}O_5$ and $Ni_5Fe(SCH_3)_{12}O_5$:Fe. Substituting a Ni atom into $Pd_6(SCH_3)_{12}$ reduced U_{onset} of the organometallic complex by ~0.45 V (Table 4) and changed the PDS from OH_{ads} formation (step I) to O_{ads} formation (step II). Nickel substitution into $Rh_6(SCH_3)_{12}$ also reduced U_{onset} by ~0.29 V while keeping the PDS unchanged, and the U_{onset} of $Rh_5Ni(SCH_3)_{12}$ is comparable to that of $Ni_6(SCH_3)_{12}$. The enhanced overpotential can be explained in terms of the overall affinity of active sites for adsorbed intermediates compared to that in the pure complexes. Nickel sites surrounded by Pd (Rh) exhibit increased (decreased) affinity for OER intermediates, resulting in a shift of their binding energies toward that of $Ni_6(SCH_3)_{12}O_5$ (see Fig. 4 in Ref [42]).

On the other hand, Fe substitution in $Ni_6(SCH_3)_{12}$ *increased* U_{onset} by 0.18 V when Ni was the active site. An even larger U_{onset} of 2.70 V was found when Fe was an active site (see Table 4), and is actually close to that of $Fe_6(SCH_3)_{12}$. These results suggest that in a mixed Ni-Fe small organometallic complex, the active site is a Ni atom away from Fe. We point out that this prediction is contrary to mixed Ni-Fe oxyhydroxides, where Fe rather than Ni constitutes the active

site for the OER [35]. Finally, substituting Fe atoms into small, organometallic Ni complexes does not appear to have the same influence that has been observed with thin-films [35] and bulk materials [54]. Note that a particular characteristic with these thin-films and bulk materials is the presence of edge-sharing [FeO_6] or [NiO_6] octahedra which is absent in the organometallic complex. These structural arrangements are responsible in the near optimal adsorption energies for OER reactive species at Fe sites and low overpotential. Doping $Ni_6(SCH_3)_{12}$ with Fe altered the binding energies of the OER intermediates. These intermediates adsorbed too strongly resulting in an increase of the overpotential. This increased affinity of the active sites is accompanied by an average bond length contraction of 2.79 % for Fe-O and 1.91% for Ni-O with respect to the pure complexes. Moreover, Fe dopant creates states in the band gap. A majority and minority Fe 3d peak appear right above the Fermi level of $Ni_5Fe(SCH_3)_{12}O_5$:Fe. Likewise one minority Fe 3d peak appears below the Fermi level of $Ni_5Fe(SCH_3)_{12}O_5$:Ni (see Fig. 6 in Ref [42]).

Overall, our results indicate that Ni substitution into small organometallic complexes can reduce the overpotentials for anodic water oxidation and therefore reduce the energy requirement, fundamental aspects of the design principles for high-efficiency OER catalysts.

4. Conclusions

Using DFT in conjunction with thermochemistry analysis we modeled a series of organometallic complexes $M_6(SCH_3)_{12}$ (M = Fe, Pd, Rh), studied their OER activity and compared it to that of our previous work on Ni complex. The calculated structural geometries are in very good agreement with available experiments. The reactive surfaces of these complexes are predicted to be oxygen-covered [$M_6(SCH_3)_{12}$-O_5] at OER potentials with one metal cation left vacant to represent the active site. Overall, our results predict the onset potential to increase as Ni < Rh < Pd < Fe. The difference in OER activity is established through adsorption energies and ring

diameter of the oxidized complexes. We find that the OER activity versus the diameter of the hexagonal ring shows a maximum at Ni complex. We also find an existence of linear correlations of the adsorption energies with the ring diameter of the oxidized complexes. Doping these complexes with Ni lowers their overpotentials and therefore increases their OER activity. The enhanced overpotential is due to the change of overall affinity of active sites for adsorbed intermediates resulting in a shift of their binding energies. We also studied the activity of Fe-doped Ni complex and our findings show that Fe incorporation into smaller Ni clusters actually decreases OER activity.

Acknowledgments

This technical effort was performed in support of the National Energy Technology Laboratory's ongoing research under the RES contract DE-FE0004000.

This project was funded by the Department of Energy, National Energy Technology Laboratory, an agency of the United States Government, through a support contract with AECOM. Neither the United States Government nor any agency thereof, nor any of their employees, nor AECOM, nor any of their employees, makes any warranty, expressed or implied, or assumes any legal liability or responsibility for the accuracy, completeness, or usefulness of any information, apparatus, product, or process disclosed, or represents that its use would not infringe privately owned rights. Reference herein to any specific commercial product, process, or service by trade name, trademark, manufacturer, or otherwise, does not necessarily constitute or imply its endorsement, recommendation, or favoring by the United States Government or any agency thereof. The views and opinions of authors expressed herein do not necessarily state or reflect those of the United States Government or any agency thereof.

References

[1] M.G. Walter, E.L. Warren, J.R. McKone, S.W. Boettcher, Q. Mi, E.A. Santori, N.S. Lewis, Solar Water Splitting Cells, Chem. Rev. 110 (2010) 6446-6473.
[2] J. Suntivich, K.J. May, H.A. Gasteiger, J.B. Goodenough, Y. Shao-Horn, A Perovskite Oxide Optimized for Oxygen Evolution Catalysis from Molecular Orbital Principles, Science 334 (2011) 1383-1385.
[3] C.C.L. McCrory, S. Jung, J.C. Peters, T.F. Jaramillo, Benchmarking Heterogeneous Electrocatalysts for the Oxygen Evolution Reaction, J. Am. Chem. Soc. 135 (2013) 16977-16987.
[4] J. Jin, K. Walczak, M.R. Singh, C. Karp, N.S. Lewis, C. Xiang, An experimental and modeling/simulation-based evaluation of the efficiency and operational performance characteristics of an integrated, membrane-free, neutral pH solar-driven water-splitting system, Energy Environ. Sci. 7 (2014) 3371-3380.
[5] H. Hakkinen, The gold-sulfur interface at the nanoscale, Nat. Chem. 4 (2012) 443-455.
[6] A. Desireddy, B.E. Conn, J. Guo, B. Yoon, R.N. Barnett, B.M. Monahan, K. Kirschbaum, W.P. Griffith, R.L. Whetten, U. Landman, T.P. Bigioni, Ultrastable silver nanoparticles, Nature 501 (2013) 399-402.
[7] A. Das, Z. Han, W.W. Brennessel, P.L. Holland, R. Eisenberg, Nickel Complexes for Robust Light-Driven and Electrocatalytic Hydrogen Production from Water, ACS Catal. 5 (2015) 1397-1406.
[8] R. Angamuthu, E. Bouwman, Reduction of protons assisted by a hexanuclear nickel thiolate metallacrown: protonation and electrocatalytic dihydrogen evolution, Phys. Chem. Chem. Phys. 11 (2009) 5578-5583.
[9] H.N. Kagalwala, E. Gottlieb, G. Li, T. Li, R. Jin, S. Bernhard, Photocatalytic Hydrogen Generation System Using a Nickel-Thiolate Hexameric Cluster, Inorg. Chem. 41 (2013) 9094-9101.
[10] W. Zhang, J. Hong, J. Zheng, Z. Huang, J. Zhou, R. Xu, Nickel−Thiolate Complex Catalyst Assembled in One Step in Water for Solar H_2 Production, J. Am. Chem. Soc. 133 (2011) 20680-20683.
[11] M.L. Helm, M.P. Stewart, R.M. Bullock, M.R. DuBois, D.L. DuBois, A Synthetic Nickel Electrocatalyst with a Turnover Frequency Above 100,000 s^{-1} for H_2 Production, Science 333 (2011) 863-866.
[12] O.R. Luca, J.D. Blakemore, S.J. Konezny, J.M. Praetorius, T.J. Schmeier, G.B. Hunsinger, V.S. Batista, G.W. Brudvig, N. Hazari, R.H. Crabtree, Organometallic Ni Pincer Complexes for the Electrocatalytic Production of Hydrogen, Inorg. Chem. 51 (2012) 8704-8709.
[13] D.R. Kauffman, D. Alfonso, D.N. Tafen, J. Lekse, C. Wang, X. Deng, J. Lee, H. Jang, J.-s. Lee, S. Kumar, C. Matranga, Electrocatalytic Oxygen Evolution with an Atomically Precise Nickel Catalyst, ACS Catal. 6 (2016) 1225-1234.
[14] N. Kunchur, The crystal structure of palladium n-propyl mercaptide, Acta Cryst. B 24 (1968) 1623-1633.
[15] J. Chen, L. Liu, L. Weng, Y. Lin, L. Liao, C. Wang, J. Yang, Z. Wu, Synthesis and Properties Evolution of a Family of Tiara-like Phenylethanethiolated Palladium Nanoclusters, Sci. Rep. 5 (2015) 16628.

[16] J. Wang, F. Jian, B. Huang, Z. Bai, Two molecular wheels 12-MC-6 complexes: Synthesis, structure and magnetic property of [Co(μ2-SEt)2]6 and [Fe(μ2-SEt)2]6, J. Solid State Chem. 204 (2013) 272-277.
[17] P. Alemany, R. Hoffmann, Toroidal nickel thiolates: structure and bonding, J. Am. Chem. Soc. 115 (1993) 8290-8297.
[18] Z. Yang, A.B. Smetana, C.M. Sorensen, K.J. Klabunde, Synthesis and Characterization of a New Tiara Pd(II) Thiolate Complex, $[Pd(SC_{12}H_{25})_2]_6$, and Its Solution-Phase Thermolysis to Prepare Nearly Monodisperse Palladium Sulfide Nanoparticles, Inorg. Chem. 46 (2007) 2427-2431.
[19] S. Rojas, J.L.G. Fierro, R. Fandos, A. Rodriguez, P. Terreros, Synthesis, structure and hydroformylation activity of monomer rhodium and iridium pyrimidine thiolate complexes, J. Chem. Soc. Dalton Trans. (2001) 2316-2324.
[20] M. Sakamoto, Y. Ohki, G. Kehr, G. Erker, K. Tatsumi, Catalytic hydrogenation of CO and CN bonds via heterolysis of H_2 mediated by metal–sulfur bonds of rhodium and iridium thiolate complexes, J. Organomet. Chem. 694 (2009) 2820-2824.
[21] Y. Misumi, H. Seino, Y. Mizobe, Heterolytic Cleavage of Hydrogen Molecule by Rhodium Thiolate Complexes That Catalyze Chemoselective Hydrogenation of Imines under Ambient Conditions, J. Am. Chem. Soc. 131 (2009) 14636-14637.
[22] P. Liao, J.A. Keith, E.A. Carter, Water Oxidation on Pure and Doped Hematite (0001) Surfaces: Prediction of Co and Ni as Effective Dopants for Electrocatalysis, J. Am. Chem. Soc. 134 (2012) 13296-13309.
[23] M. García-Mota, A. Vojvodic, H. Metiu, I.C. Man, H.-Y. Su, J. Rossmeisl, J.K. Nørskov, Tailoring the Activity for Oxygen Evolution Electrocatalysis on Rutile TiO_2(110) by Transition-Metal Substitution, ChemCatChem 3 (2011) 1607-1611.
[24] A. Kay, I. Cesar, M. Grätzel, New Benchmark for Water Photooxidation by Nanostructured α-Fe2O3 Films, J. Am. Chem. Soc. 128 (2006) 15714-15721.
[25] G. Kresse, J. Furthmüller, Efficiency of ab-initio Total Energy Calculations for Metals and Semiconductors Using a Plane-Wave Basis Set, Comp. Mat. Sci. 6 (1996) 15-50.
[26] G. Kresse, J. Hafner, Norm-Conserving and Ultrasoft Pseudopotentials for First-Row and Transition Elements, J. Phys.: Condens. Matter 6 (1994) 8245-8257.
[27] J.P. Perdew, K. Burke, M. Ernzerhof, Generalized Gradient Approximation Made Simple, Phys. Rev. Lett. 77 (1996) 3865-3868.
[28] G. Kresse, D. Joubert, From Ultrasoft Pseudopotentials to the Projector Augmented-Wave Method, Phys. Rev. B 59 (1999) 1758-1775.
[29] O. Lopez-Acevedo, K.A. Kacprzak, J. Akola, H. Häkkinen, Quantum Size Effects in Ambient CO Oxidation Catalysed by Ligand-Protected Gold Clusters, Nat. Chem. 2 (2010) 329-334.
[30] Y. Negishi, W. Kurashige, Y. Niihori, T. Iwasa, K. Nobusada, Isolation, Structure, and Stability of a Dodecanethiolate-Protected Pd_1Au_{24} cluster, Phys. Chem. Chem. Phys. 12 (2010) 6219-6225.
[31] J. Rossmeisl, Z.-W. Qu, H. Zhu, G.-J. Kroes, J.K. Nørskov, Electrolysis of Water on Oxide Surfaces, J. Electroanal. Chem. 607 (2007) 83-89.
[32] Á. Valdés, Z.-W. Qu, G.-J. Kroes, Oxidation and Photo-Oxidation of Water on TiO_2 Surface, J. Phys. Chem. C 112 (2008) 9872-9879.

[33] I.C. Man, H.-Y. Su, F. Calle-Vallejo, H.A. Hansen, J.I. Martínez, N.G. Inoglu, J. Kitchin, T.F. Jaramillo, J.K. Nørskov, J. Rossmeisl, Universality in Oxygen Evolution Electrocatalysis on Oxide Surfaces, ChemCatChem 7 (2011) 1159-1165.
[34] M. Bajdich, M. García-Mota, A. Vojvodic, J.K. Nørskov, A.T. Bell, Theoretical Investigation of the Activity of Cobalt Oxides for the Electrochemical Oxidation of Water, J. Am. Chem. Soc. 135 (2013) 13521-13530.
[35] D. Friebel, M.W. Louie, M. Bajdich, K.E. Sanwald, Y. Cai, A.M. Wise, M.-J. Cheng, D. Sokaras, T.-C. Weng, R. Alonso-Mori, R.C. Davis, J.R. Bargar, J.K. Nørskov, A. Nilsson, A.T. Bell, Identification of Highly Active Fe Sites in (Ni,Fe)OOH for Electrocatalytic Water Splitting, J. Am. Chem. Soc. 137 (2015) 1305-1313.
[36] J.K. Nørskov, J. Rossmeisl, A. Logadottir, L. Lindqvist, J.R. Kitchin, T. Bligaard, H. Jónsson, Origin of the Overpotential for Oxygen Reduction at a Fuel-Cell Cathode, J. Phys. Chem. B 108 (2004) 17886-17892.
[37] Q. Tang, Y. Lee, D.-Y. Li, W. Choi, C.W. Liu, D. Lee, D.-e. Jiang, Lattice-Hydride Mechanism in Electrocatalytic CO_2 Reduction by Structurally Precise Copper-Hydride Nanoclusters, J. Am. Chem. Soc. 139 (2017) 9728-9736.
[38] D.W. Blaylock, T. Ogura, W.H. Green, G.J.O. Beran, Computational Investigation of Thermochemistry and Kinetics of Steam Methane Reforming on Ni(111) under Realistic Conditions, J. Phys. Chem. C 113 (2009) 4898-4908.
[39] C.J. Cramer, Essentials of Computational Chemistry: Theories and Models, Wiley, 2004.
[40] M. Fishman, H.L. Zhuang, K. Mathew, W. Dirschka, R.G. Hennig, Accuracy of Exchange-Correlation Functionals and Effect of Solvation on the Surface Energy of Copper, Phys. Rev. B 87 (2013) 245402.
[41] K. Mathew, R. Sundararaman, K. Letchworth-Weaver, T.A. Arias, R.G. Hennig, Implicit Solvation Model for Density-Functional Study of Nanocrystal Surfaces and Reaction Pathways, J. Chem. Phys. 140 (2014) 084106.
[42] D.N. Tafen, D.R. Kauffman, D.R. Alfonso, Data set for electrocatalytic oxygen evolution with pure and substituted $M_6(SR)_{12}$ (M = Pd, Fe, Rh) complexes from computational techniques, Data in Brief, (2018) Submitted for publication.
[43] J. Rossmeisl, A. Logadottir, J.K. Nørskov, Electrolysis of Water on (Oxidized) Metal Surfaces, Chem. Phys. 319 (2005) 178-184.
[44] J. Heyd, G.E. Scuseria, M. Ernzerhof, Hybrid functionals based on a screened Coulomb potential, J. Chem. Phys. 118 (2003) 8207-8215.
[45] B. Hammer, J.K. Norskov, Why gold is the noblest of all the metals, Nature 376 (1995) 238-240.
[46] L.G.M. Pettersson, A. Nilsson, A Molecular Perspective on the d-Band Model: Synergy Between Experiment and Theory, Top. Catal. 57 (2013) 2-13.
[47] P. Sabatier, La catalyse en chimie organique, Librairie Polytechnique, Paris et Liege, 1920.
[48] M. Che, Nobel Prize in chemistry 1912 to Sabatier: Organic chemistry or catalysis?, Catal. Today, 218–219 (2013) 162-171.
[49] F. Calle-Vallejo, N.G. Inoglu, H.-Y. Su, J.I. Martinez, I.C. Man, M.T.M. Koper, J.R. Kitchin, J. Rossmeisl, Number of outer electrons as descriptor for adsorption processes on transition metals and their oxides, Chem. Sci. 4 (2013) 1245-1249.
[50] M. Mavrikakis, B. Hammer, J.K. Nørskov, Effect of Strain on the Reactivity of Metal Surfaces, Phys. Rev. Lett. 81 (1998) 2819-2822.

[51] F. Calle-Vallejo, J. Tymoczko, V. Colic, Q.H. Vu, M.D. Pohl, K. Morgenstern, D. Loffreda, P. Sautet, W. Schuhmann, A.S. Bandarenka, Finding optimal surface sites on heterogeneous catalysts by counting nearest neighbors, Science 350 (2015) 185.
[52] M. Escudero-Escribano, P. Malacrida, M.H. Hansen, U.G. Vej-Hansen, A. Velázquez-Palenzuela, V. Tripkovic, J. Schiøtz, J. Rossmeisl, I.E.L. Stephens, I. Chorkendorff, Tuning the activity of Pt alloy electrocatalysts by means of the lanthanide contraction, Science 352 (2016) 73-76.
[53] G. Henkelman, A. Arnaldsson, H. Jónsson, A fast and robust algorithm for Bader decomposition of charge density, Comp. Mat. Sci. 36 (2006) 354-360.
[54] L. Trotochaud, S.L. Young, J.K. Ranney, S.W. Boettcher, Nickel−Iron Oxyhydroxide Oxygen-Evolution Electrocatalysts: The Role of Intentional and Incidental Iron Incorporation, J. Am. Chem. Soc. 136 (2014) 6744−6753.